

Iterative Inversion of Deformation Vector Fields with Feedback Control

Abhishek Kumar Dubey^{*}, Alexandros-Stavros Iliopoulos^{*}, Xiaobai Sun^{*}, Fang-Fang Yin[†], and Lei Ren[†]

^{*}Department of Computer Science, Duke University, Durham, NC 27705, USA

[†]Department of Radiation Oncology, Duke University School of Medicine, Durham, NC 27710, USA

Abstract

Purpose: The inverse of a deformation vector field (DVF) is often needed in deformable registration, 4D image reconstruction, and adaptive radiation therapy. This study aims at improving both the accuracy with respect to inverse consistency and efficiency of the numerical DVF inversion by developing a fixed-point iteration method with feedback control.

Method: We introduce an iterative method with active feedback control for DVF inversion. The method is built upon a previous fixed-point iteration method, which is represented as a particular passive instance in the new method. At each iteration step, we measure the inconsistency, namely the residual, between the iterative inverse estimate and the input DVF. The residual is modulated by a feedback control mechanism before being incorporated into the next iterate. The feedback control design is based on analysis of error propagation in the iteration process. The control design goal is to suppress estimation error progressively to make the convergence region as large as possible, and to make estimate errors vanish faster whenever possible. We demonstrated the feedback control with a single-parameter control mechanism. The optimal parameter value is determined either analytically by a closed-form expression for analytical test data, or numerically for experimental data. The feedback control design is demonstrated and assessed with two data sets: an analytic DVF pair, and a DVF generated between two phases of the 4D Extended Cardiac-Torso (XCAT) digital anthropomorphic phantom.

Results: The single-parameter feedback control improved both the convergence region and convergence rate of the iterative algorithm, for both datasets. With the analytic data, the iteration becomes convergent over the entire image domain, and the convergence is sped up substantially compared to the precursor method, which suffers from slow convergence or even divergence, as the deformation becomes larger. With the XCAT DVF data, the new iteration method substantially outperforms the precursor method in both accuracy and efficiency; feedback control reduced the 95th percentile of residual errors from 1 mm to 10^{-6} mm. Additionally, convergence rate was accelerated by at least a factor of 2 for both datasets.

Conclusion: The introduced iteration method for DVF inversion shows the previously unexplored possibility in exercising active feedback control in DVF inversion, and the unexploited potential in improving both numerical accuracy and computational efficiency.

1 Introduction

We consider numerical inversion of a forward deformation vector field (DVF) from one image to another. Very often the inverse DVF is needed along with the forward DVF to map medical images, structures, or doses back and forth throughout the process of 4D image reconstruction and adaptive radiotherapy [5, 9]. The inverse DVF may be obtained in different ways, such as through deformable registration with swapped inputs, simultaneous registration in both directions, or inverting the forward DVF from the reference image to the deformed target image. The latter option (inverting the forward DVF) is often preferred in clinical applications, due to several reasons: (i) inversion is typically faster, empir-

ically; (ii) image quality can be quite different for the reference and target image sets, which may make the other approaches more error-prone [4]; and (iii) inversion can ensure consistency between forward and inverse DVFs [8]. Previously, Chen *et al.* [1] developed a fixed-point iteration method for DVF inversion. In this study, we aim to advance the DVF inversion approach further by improving its convergence behavior, in terms of convergence region and rate, using a feedback control.

The problem of DVF inversion can be framed as follows. The reference and target images, denoted by \mathcal{R} and \mathcal{T} , respectively, can be related to one another by two non-linear transformations. The forward transformation, $f : \mathcal{R} \rightarrow \mathcal{T}$, maps the voxels of the reference

image, \mathcal{R} , onto those of the target image, \mathcal{T} , via the forward deformation vector field, \mathbf{F} :

$$f(\mathbf{x}) = \mathbf{F}(\mathbf{x}) + \mathbf{x}, \quad \mathbf{x} \in \Omega, \quad (1)$$

where $\mathbf{F}(\mathbf{x})$ is the 3D displacement of the reference voxel at \mathbf{x} , and Ω is the image domain. Conversely, the backward transformation, $g : \mathcal{T} \rightarrow \mathcal{R}$, maps the voxels of \mathcal{T} back to \mathcal{R} ,

$$g(\mathbf{x}') = \mathbf{G}(\mathbf{x}') + \mathbf{x}', \quad \mathbf{x}' \in \Omega, \quad (2)$$

via \mathbf{G} , the reverse DVF. The problem of DVF inversion is to obtain \mathbf{G} given \mathbf{F} . The two transformations are the inverse of each other, i.e.,

$$(g \circ f)(\mathcal{R}) = \mathcal{R}, \quad (f \circ g)(\mathcal{T}) = \mathcal{T}. \quad (3)$$

Consequently, the forward and backward DVFs satisfy the *simultaneous inverse consistency condition*:

$$\mathbf{F}(\mathbf{x}) + \mathbf{G}(\mathbf{x} + \mathbf{F}(\mathbf{x})) = 0, \quad (4a)$$

$$\mathbf{G}(\mathbf{x}') + \mathbf{F}(\mathbf{x}' + \mathbf{G}(\mathbf{x}')) = 0, \quad (4b)$$

where $\mathbf{x}, \mathbf{x}' \in \Omega$.

Inverse consistency is of great importance to deformable registration and estimation of 4D dose accumulation, among other biomedical applications [2, 8]. The inverse consistency condition is commonly incorporated in deformable registration processes. For instance, Christensen and Johnson [2] formulate image registration using objective functions symmetrically between the two images in both matching and regularization terms. Leow *et al.* [3] also treat the two images symmetrically, and use inverse consistency in approximating the unknown inverse fields. Additional related studies on employing the consistency condition in simultaneous estimates of the forward and inverse DVF can be found in the survey by Sotiras *et al.* [8].

The study reported in this paper follows and improves upon the work of Chen *et al.* [1]. The precursor work presented a fixed-point iteration method for DVF inversion, with regard to inverse consistency condition. The significance of that work lies not only in the simple iterative process, but also in the corresponding convergence condition. Assuming \mathbf{F} is given, Chen's iteration proceeds as,

$$\hat{\mathbf{G}}_{k+1}(\mathbf{x}) = -\mathbf{F}(\mathbf{x} + \hat{\mathbf{G}}_k(\mathbf{x})). \quad (5)$$

The initial guess, $\hat{\mathbf{G}}_0$, is set to zero; i.e., $\hat{\mathbf{G}}_1 = -\mathbf{F}$. Negating the forward DVF used to a prevailing approach for inverse DVF computation, but the resulting inverse estimate, $\hat{\mathbf{G}}_1$, does not in general satisfy inverse consistency. This common misconception was made clear and amended by the fixed-point iteration solution of (5). With fixed-point method, the convergence behavior of the iterative inversion process can be analyzed, which is

a substantial advancement from previous methods which solely relied on empirical studies. A sufficient convergence condition for (5) is the contraction condition on \mathbf{F} :

$$d(\mathbf{F}(\mathbf{x}), \mathbf{F}(\mathbf{x}')) \leq \alpha d(\mathbf{x}, \mathbf{x}'), \quad \forall \mathbf{x}, \mathbf{x}' \in \Omega, \quad (6)$$

where d is a well-defined distance metric in the 3D image domain, and α is a Lipschitz constant, $0 \leq \alpha < 1$. The convergence behavior of Chen's iteration depends passively on this condition, which is not always met in clinical cases with large deformation.

In this study, we introduce an iterative method with an active feedback control mechanism. At each step of the iteration, we compute a residual which measures the inconsistency between the forward DVF and the iterative inverse estimate, see (7). The residual is incorporated into the next iterate after being modulated by the feedback control. The feedback control provides an extra handle for controlling and improving the convergence behavior.

The rest of the document is organized as follows. In Section 2, we describe the new iterative method with feedback control, introduce a simple feedback control mechanism, and provide the underlying principle. In Section 3, we make experimental assessment of the new method with an analytic DVF pair and with numerical DVFs obtained via the 4D Extended Cardiac-Torso (XCAT) digital anthropomorphic phantom [6]. In Section 4, we conclude the presented work and give additional remarks on extended feedback control.

2 Materials and methods

An iterative method with feedback control is first introduced for numerical DVF inversion. An analysis is then provided for steering the feedback mechanism to improve convergence behavior.

2.1 Iterative methods with feedback control

At each iteration step, we get an iterative estimate, $\hat{\mathbf{G}}$, of the inverse DVF, \mathbf{G} . We use the residual with respect to the consistency condition of (4) as the feedback:

$$\mathbf{R}(\mathbf{x}) = \hat{\mathbf{G}}(\mathbf{x}) + \mathbf{F}(\mathbf{x} + \hat{\mathbf{G}}(\mathbf{x})). \quad (7)$$

The residual can be obtained at each iteration step. This computationally available quantity allows us to monitor and control the (unknown) estimate error,

$$\mathbf{E}(\mathbf{x}) = \hat{\mathbf{G}}(\mathbf{x}) - \mathbf{G}(\mathbf{x}), \quad (8)$$

which is to be reduced to zero, or sufficiently close to zero, via the iteration process. The residual \mathbf{R} is small when the error \mathbf{E} is small, and \mathbf{E} is zero when $\hat{\mathbf{G}}$ is equal to the inverse satisfying the consistency condition (4).

Feedback control is introduced in the iteration process as follows. The residual for the k -th iterate, $\hat{\mathbf{R}}_k$, is calculated, modulated by a nonsingular matrix \mathbf{B} , and used as an incremental correction,

$$\hat{\mathbf{G}}_{k+1}(\mathbf{x}) = \hat{\mathbf{G}}_k(\mathbf{x}) - \mathbf{B}(\mathbf{x}) \mathbf{R}_k(\mathbf{x}), \quad (9)$$

where $\mathbf{B}(\mathbf{x})$ is a 3×3 matrix, local to each $\mathbf{x} \in \Omega$. Feedback control is spatially homogeneous when \mathbf{B} does not vary with \mathbf{x} . There are many formulations or reformulations of a fixed-point equation. The formulation in (9) is a general formulation for fixed-point iterations, with feedback control \mathbf{B} modifying and transforming the residual before it is fed back to $\hat{\mathbf{G}}_{k+1}$.

In this study, we focus on the feedback mechanism in its simplest form—with a single parameter. We let $\mathbf{B} = (1 - \mu)\mathbf{I}$, where \mathbf{I} is the identity matrix, and μ is a scalar which may be referred to as the relaxation parameter. The iteration process thus takes the simple form:

$$\hat{\mathbf{G}}_{k+1}(\mathbf{x}) = \hat{\mathbf{G}}_k(\mathbf{x}) - (1 - \mu) \mathbf{R}_k(\mathbf{x}). \quad (10)$$

When $\mu = 0$, the iteration of (10) reduces to Chen's iteration of (5). Hereafter, we refer to the iteration procedure by Chen *et al.* as the iteration with feedback control $\mu = 0$.

2.2 Design of feedback control

2.2.1 Feedback control for inversion of analytic DVFs

We first demonstrate how the feedback control can be designed for inverting the analytic DVFs introduced by Chen *et al.* [1]. The forward and backward DVFs are expressed by the following closed-form formulas over a 2D spatial domain:

$$\mathbf{F}(\mathbf{x}) = \left(\frac{1}{1 + b \cos(m\theta)} - 1 \right) \mathbf{x}, \quad (11a)$$

$$\mathbf{G}(\mathbf{x}) = b \cos(m\theta) \mathbf{x}, \quad (11b)$$

where \mathbf{x} denotes Cartesian coordinates in the 2D spatial domain $\Omega = [-30, 30]^2$, and θ is the corresponding angular coordinate in the polar representation, $\mathbf{x}^T = \|\mathbf{x}\|(\cos(\theta), \sin(\theta))$. The DVF functions have two constant parameters, b and m . Fig. 1 illustrates a source image and two target images; the latter are related to the former by the analytic DVFs of (11). It is straightforward to verify that the analytic DVFs satisfy the consistency condition of (4).

When $b = 0$, there is no deformation. When $m = 0$ and $b > 0$, the displacement (forward or backward) at \mathbf{x} is proportional to \mathbf{x} . With $m \neq 0$ and $b \neq 0$, the deformation at \mathbf{x} remains in the radial direction, but its magnitude varies with b and $m\theta$; when b is close to or larger than 0.5, the deformation becomes large at and near angles where $\cos(m\theta) = -1$. The iteration with control $\mu = 0$ converges slowly when b approaches 0.5

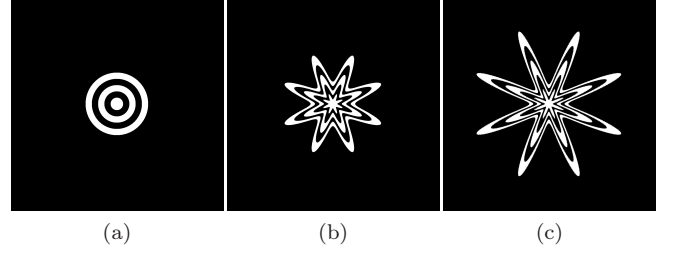


Figure 1: Sample images for illustrating deformations with the analytic DVFs of (11). (a) Reference image. (b) Deformed image using the analytic DVF with $m = 8$ and $b = 0.4$. (c) Deformed image using the analytic DVF with $m = 8$ and $b = 0.6$.

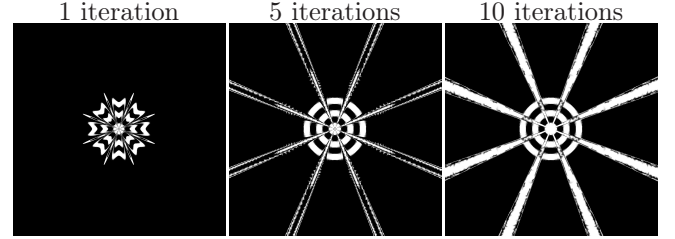


Figure 2: Constructed reference image Fig. 1a obtained by deforming target image Fig. 1c with the inverse DVF estimate of the iteration with $\mu = 0$ after 1, 5 and 10 iteration steps. Divergence regions can be seen around $\theta = (2k + 1)\frac{\pi}{8}$.

from below, and becomes divergent when b is greater than 0.5. In fact, the contraction condition (6) no longer holds at all θ values when $b > 0.5$.

To improve convergence, we begin by taking a closer look at how errors propagate through the iteration process. Errors in two successive iteration steps are related by the following propagation equation:

$$\mathbf{E}_{k+1}(\mathbf{x}) = \left[1 - (1 - \mu) \frac{1}{1 + b \cos(m\theta)} \right] \cdot \mathbf{E}_k(\mathbf{x}). \quad (12)$$

Our objective is to suppress the iterative error (12) at every step and make it vanish at a faster pace. When $\mu = 0$ and $b > 0.5$, the error propagation factor is greater than one at and near angular locations where $\cos(m\theta) = -1$. Wherever the factor is greater than 1, the iterative errors are magnified instead of suppressed at each iteration. This explains the divergent behavior with $\mu = 0$ at certain polar angles when $b > 0.5$, as illustrated in Fig. 2. When $\mu = 0$ and $b < 0.5$, the propagation factor is less than 1 at any θ , and the iteration converges in theory. But as b approaches to 0.5 from below, the iteration becomes slower.

Further analysis, provided in Appendix C, shows that the single-parameter feedback control can be employed to achieve convergence over the entire image domain with this analytic DVF pair. We claim specifically that, for any $b \in (0, 1)$, there exists some $\mu \in [0, 1)$ which satisfies the following necessary and sufficient convergence

condition:

$$\mu > 2b - 1. \quad (13)$$

Under this condition, the iteration (10) converges over the entire image domain for any $b \in (0, 1)$, with arbitrary initial guess. For $b \geq 0.5$, iteration with the feedback control $\mu = 0$ fails to meet the necessary and sufficient condition.

Among the feasible values for the parameter μ , one may find, by the propagation factor in (12), that some values of μ render faster convergence than others. In particular, we find the optimal value,

$$\mu_{\text{opt}} = b^2. \quad (14)$$

We provide the proofs of (12), (13) and (14) in Appendices A, C and D.

2.2.2 Feedback control principle

In this section, we will describe the basic principle, objectives and approach for feedback control, taking into consideration that, in practice, the forward DVF is provided in numerical values over a discrete spatial domain, not in a closed-form expression.

The design of feedback control is based in principle on the error propagation analysis. For the iteration of (10) with a single control parameter μ , the error propagation equation may be described in the first order form,

$$\mathbf{E}_{k+1}(\mathbf{x}) = \mathbf{P}(\mu, \mathbf{x}) \cdot \mathbf{E}_k(\mathbf{x}), \quad (15a)$$

$$\mathbf{P}(\mu, \mathbf{x}) = \mathbf{I} - (1 - \mu)(\mathbf{I} + \mathbf{J}_{\mathbf{F}}(\tilde{\mathbf{x}})), \quad (15b)$$

where \mathbf{I} is the identity matrix, $\tilde{\mathbf{x}}$ is a location in $[\mathbf{x} + \mathbf{G}(\mathbf{x}), \mathbf{x} + \hat{\mathbf{G}}_k(\mathbf{x})]$, $\mathbf{J}_{\mathbf{F}}(\tilde{\mathbf{x}})$ denotes the Jacobian of \mathbf{F} evaluated at $\tilde{\mathbf{x}}$, and $\mathbf{P}(\mu, \mathbf{x})$ denotes the error propagation matrix. In order to express the error propagation matrix in a first-order form, we assume that \mathbf{F} is smooth almost everywhere over the spatial domain and the Jacobian can be well approximated from the numerical values of \mathbf{F} .

The first control objective is to make the propagation matrix \mathbf{P} a contractor over the image domain of interest, which implies that the convergence region must span the entire image domain. When the feedback control, $\mathbf{B}(\mathbf{x})$, is limited by a specific mechanism structure, one may consider making the convergence region in the image domain as large as possible. The second objective is to make the convergence as fast as possible.

We describe in particular the control design approach with the single-parameter control mechanism. First, we find the feasible values of μ over which \mathbf{P} is a contractor over the spatial domain of interest,

$$\rho(\mathbf{P}(\mu, \mathbf{x})) \leq 1, \quad (16)$$

where ρ is the spectral radius of the propagation matrix. If the feasible set is not empty, we next locate the values

of μ that reach the fastest convergence speed possible. In Section 2.2.1, we have demonstrated how to achieve these objectives with analytic DVFs. In Section 3.4, we will introduce a simple approach to locate μ in practical situation where the DVF is numerically provided, without a closed-form expression.

3 Experiments and results

We present experimental results for assessing the new iterative method. First, we will describe the data sets and assessment measures.

3.1 Data sets

Two particular sets, referred to as set A and set B for convenience, were used for evaluating the single-parameter feedback control process of (10).

Data set A is analytically designed by Chen *et al.* [1]. It includes a reference image and a deformed (target) image, in 2D, as shown in Fig. 1. The reference image is binary-valued; the intensity is one over the concentric rings, and 0 otherwise. The DVF from the reference to the target image follows the analytic expression (11). In the experiments, the DVF parameter m is set to 8, and the parameter b takes values below or above 0.5 (which is the critical point for Chen's iteration from converge to diverge).

Data set B consists of two images of a digital lung phantom generated using XCAT [6]. The reference image is at the end-of-expiration phase and the target image is at the end-of-inspiration phase. The forward DVF, from the reference to the target image, was provided by XCAT. Respiratory motion was generated by two parametrized sinusoidal curves: one for diaphragm motion in the SI direction, and one for chest surface motion in the AP direction. The curve and surface parameters were set to the XCAT default values, with a 5 s respiratory cycle, and asymmetric sinusoids with respect to inspiration and expiration duration. Peak-to-peak displacements at the diaphragm and chest surface were set to 6 cm and 3 cm in SI and AP directions, respectively. The large displacements were chosen in order to test the convergence behavior of the iteration methods in a challenging condition that may be expected in a clinical scenario [7]. Voxel resolution was set to 1.67 mm in all three dimensions. The XCAT phantom deformation fields are mostly smooth over the image domain, except at certain surface boundaries, such as around the spine.

3.2 Assessment schemes

We use two kinds of schemes for assessing the effect of feedback control on convergence behavior. The first kind of scheme shows the spatial variation of errors using images or error maps. The second kind scheme uses scalar

quantities to summarize estimate errors in the worst case or in aggregation.

For dataset A, visual assessment of spatial variation of errors is materialized in two ways. In one, the proxy target and references images are constructed by the inverse DVF estimate under evaluation. In the other, a map of pixel-wise residuals is overlaid on the target image. The scalar assessment scheme comprises the maximal residual error and the maximal absolute error at each iteration,

$$R_{\max} = \max_{\mathbf{x} \in \Omega} \|\mathbf{R}(\mathbf{x})\|_2, \quad (17a)$$

$$E_{\max} = \max_{\mathbf{x} \in \Omega} \|\mathbf{E}(\mathbf{x})\|_2, \quad (17b)$$

where Ω is the image domain, $\Omega = [-30, 30]^2$.

For dataset B, the scheme for assessing the spatial variation of errors is similar to that for dataset A, except that proxy images are constructed for only the target phase, for the following reason. Unlike the ideal case with dataset A, local transforms of image voxels by the DVFs may not be one-to-one numerically, which happens to be the case with the backward transform for dataset B. This numerically ill condition makes the constructed reference images via numerical interpolation much more susceptible to numerical artifacts, especially around the outer body interface. The scalar assessment scheme is limited to the measure of residual errors, as the absolute errors are not obtainable with the exact inverse unknown. Taking into account the presence of discontinuities at certain boundaries and other sources of variation, residual errors are assessed via percentiles at different levels, defined as,

$$R(\beta) = \inf_{\mathbf{x} \in \Omega} \left\{ \|\mathbf{R}(\mathbf{x})\|_2 \mid H(\|\mathbf{R}(\mathbf{x})\|_2) \geq \beta \right\}, \quad \beta \in (0, 1), \quad (18)$$

where $H(\|\mathbf{R}(\mathbf{x})\|_2)$ is the normalized cumulative histogram of $\|\mathbf{R}(\mathbf{x})\|_2$, and the image domain Ω excludes voxels outside the body. In particular, we use percentiles with $\beta = 0.9$ and $\beta = 0.95$.

3.3 Results with analytic DVFs (set A)

We present experimental results, in Figs. 3–8, with the analytical DVF of (11), at two DVF parameter settings. The parameter m is set to 8 in both settings and b is set to 0.4 in one setting and 0.6 in the other.

When $b = 0.4$, the iteration of (10) converges for any $\mu \in [0, 1]$. Figs. 3 and 5 show the iterative estimates of the reference and target images respectively at intermediate steps of the iteration process. The iteration of (10) with feedback control $\mu = 0.16$ recovers the reference and target images in at most 5 steps, whereas the iteration with feedback control $\mu = 0$ takes more steps. A quantitative confirmation of the speedup, shown in Fig. 7, shows the comparison in convergence rate among

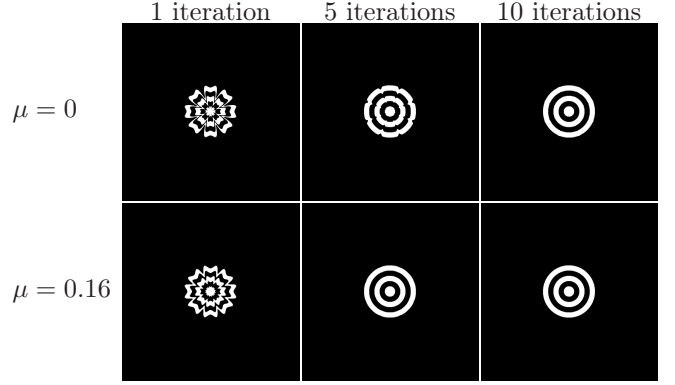


Figure 3: Constructed reference images by the estimated inverse DVF from the analytic deformed target image ($b = 0.4$ and $m = 8$). The difference from the ground truth reference image shows the effect of spatial variation in estimate errors and the control setting. The images on the left, middle and right are associated, respectively, with inverse estimates at iteration steps 1, 5 and 10; on the top and bottom are related to the iterations with the control parameter $\mu = 0$ and $\mu = 0.16$, respectively. The bottom images approach the ground truth reference image faster.

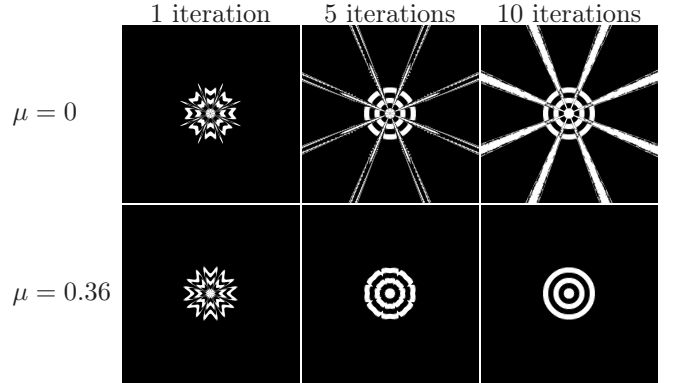


Figure 4: Constructed reference images by the estimated inverse DVF from the analytic deformed target image ($b = 0.6$ and $m = 8$). The difference from the ground truth reference image shows the effect of spatial variation in estimate errors and the control setting. The images on the left, middle and right are associated, respectively, with inverse estimates at iteration steps 1, 5 and 10; on the top and bottom are related to the iterations with the control parameter $\mu = 0$ and $\mu = 0.36$, respectively. The top images fail to converge over the entire image domain.

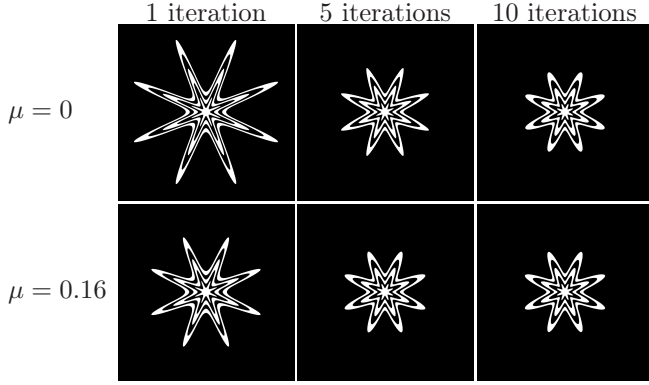


Figure 5: Constructed target images by the forward DVF corresponding to the inverse estimate. The difference from the analytic deformed target image with $b = 0.4$ and $m = 8$ shows the effect of spatial variation in estimate errors and the control setting. The images on the left, middle and right are associated, respectively, with inverse estimates at iteration steps 1, 5 and 10; on the top and bottom are related to the iterations with the control parameter $\mu = 0$ and $\mu = 0.16$, respectively. The images at the bottom approach the ground truth target faster.

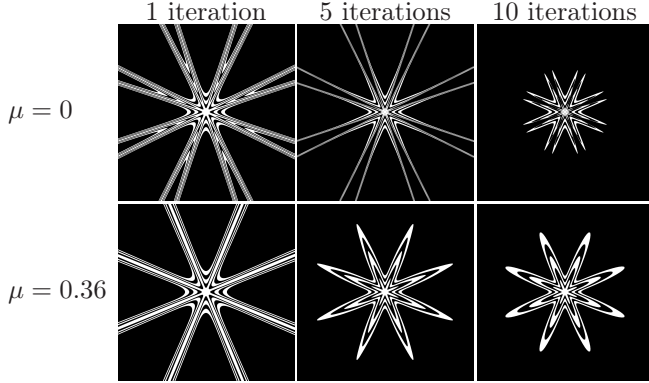


Figure 6: Constructed target images by the forward DVF corresponding to the inverse estimate. The difference from the analytic deformed target image with $b = 0.6$ and $m = 8$ shows the effect of spatial variation in estimate errors and control setting. The images on the left, middle and right are associated, respectively, with inverse estimates at iteration steps 1, 5 and 10; on the top and bottom are related to the iterations with the control parameter $\mu = 0$ and $\mu = 0.36$, respectively. The top images fail to converge to the ground truth target image.

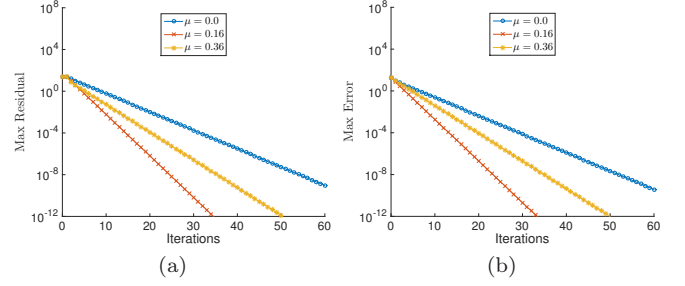


Figure 7: Comparison in convergence rate among different control settings at $\mu \in \{0, 0.16, 0.36\}$ with analytical DVF (parameters $m = 8$ and $b = 0.4$). (a) Maximal residual errors through 60 iterations; (b) Maximal absolute errors through 60 iterations; The convergence rate is increasing from $\mu = 0$ to $\mu = 0.16$.

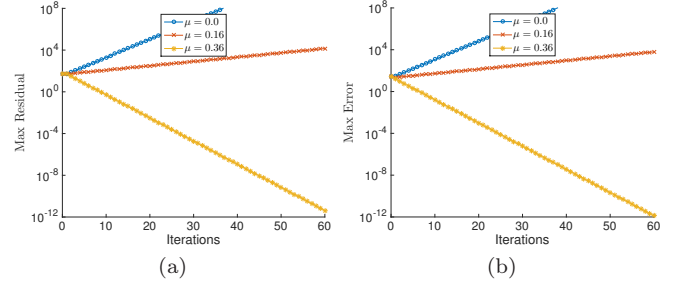


Figure 8: Comparison in convergence rate among different control settings at $\mu \in \{0, 0.16, 0.36\}$ with analytical DVF (with parameters $m = 8$ and $b = 0.6$). (a) Maximal residual errors through 60 iterations; (b) Maximal absolute errors through 60 iterations; The convergence behavior undergoes critical changes from divergence to convergence as the control parameter changes from $\mu = 0$ to $\mu = 0.36$.

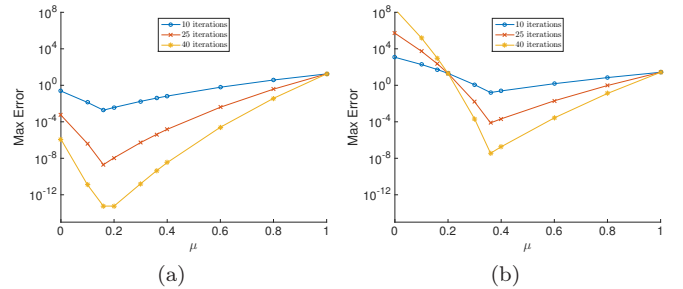


Figure 9: Locating optimal control parameter in the analytical study with (a) $b = 0.4$ and (b) $b = 0.6$. Maximal absolute errors at 10, 25 and 40 iterations are plotted against parameter $\mu \in (0, 1)$. The absolute errors are at minimum with $\mu = 0.16$ and $\mu = 0.36$ respectively for analytical DVF with $b = 0.4$ and $\mu = 0.36$, confirming the analytical result of (14).

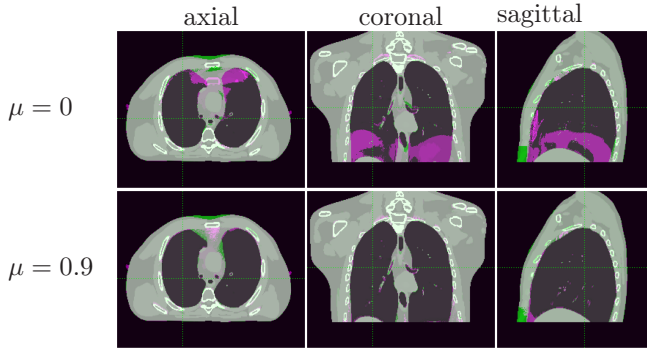


Figure 11: Constructed target image by deforming the reference image based on the inverse DVF estimates. Constructed target image is shown in magenta, whereas the ground truth target image is shown in green. The top and bottom are related to the iteration with the feedback control $\mu = 0$ and $\mu = 0.9$, respectively. The top images fail to converge to the real target image, evidenced by the large discrepancy between the constructed and the ground truth images.

the feasible values. The iteration with $\mu = 0.16$ is at least two times faster than with $\mu = 0$.

Figs. 4 and 6 show the results when the deformation is larger. The iteration with $\mu = 0$ diverges, whereas iteration with $\mu = 0.36$ recovers the reference and target images successfully in at most 10 steps. Fig. 8 shows the critical change from divergence to convergence. Figs. 7, 8 and 9 provide numerical evidence that errors decrease faster when the feedback control parameter μ is set to the analytically optimal value in (14).

3.4 Results with XCAT phantom (set B)

We present experimental results for the XCAT phantom. Fig. 10 shows residual errors overlaid on CT slices. The residual errors are much smaller with the feedback control $\mu = 0.9$, especially around the diaphragm. Fig. 11 shows the spatial distribution of errors by means of the constructed target image. The target image is constructed by deforming the reference image with inverse estimate. The constructed target image with $\mu = 0.9$ exhibits substantially smaller errors compared to that with $\mu = 0$. Fig. 12 shows the residuals $R(\beta)$ at $\beta = 0.9$ and $\beta = 0.95$ against the number of iteration steps. The residual $R(0.95)$ drops below 10^{-5} mm for iteration with feedback control ($\mu = 0.4$ and $\mu = 0.6$), whereas the same remains above 1 cm level with $\mu = 0$. Fig. 13 shows the variation of residual percentiles $R(\beta)$ with parameter μ with minima occurring at $\mu = 0.6$.

4 Conclusion & discussion

We have introduced an iterative method for numerical DVF inversion with a feedback control mechanism to

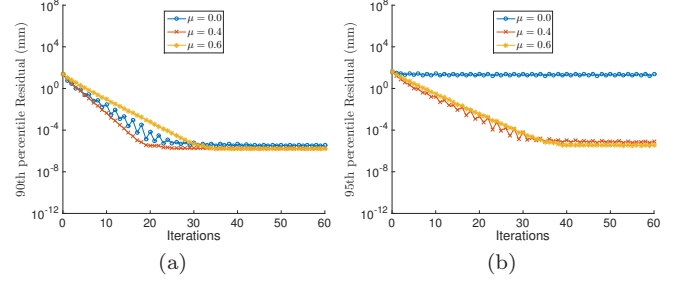


Figure 12: Convergence behavior with the XCAT phantom data. Residuals (18) with (a) $\beta = 0.9$ and (b) $\beta = 0.95$ through 60 iterations with different control parameter settings $\mu \in \{0, 0.4, 0.6\}$. Iteration with $\mu = 0.6$ is faster than with $\mu = 0$ and converges over a larger region.

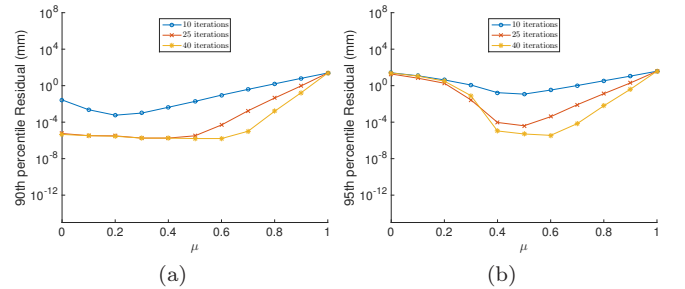


Figure 13: Locating optimal control parameter in the XCAT study. Residuals (18) with (a) $\beta = 0.9$ and (b) $\beta = 0.95$ are plotted against parameter μ for 10, 25 and 40 iterations. The residual errors are minimal at $\mu = 0.6$.

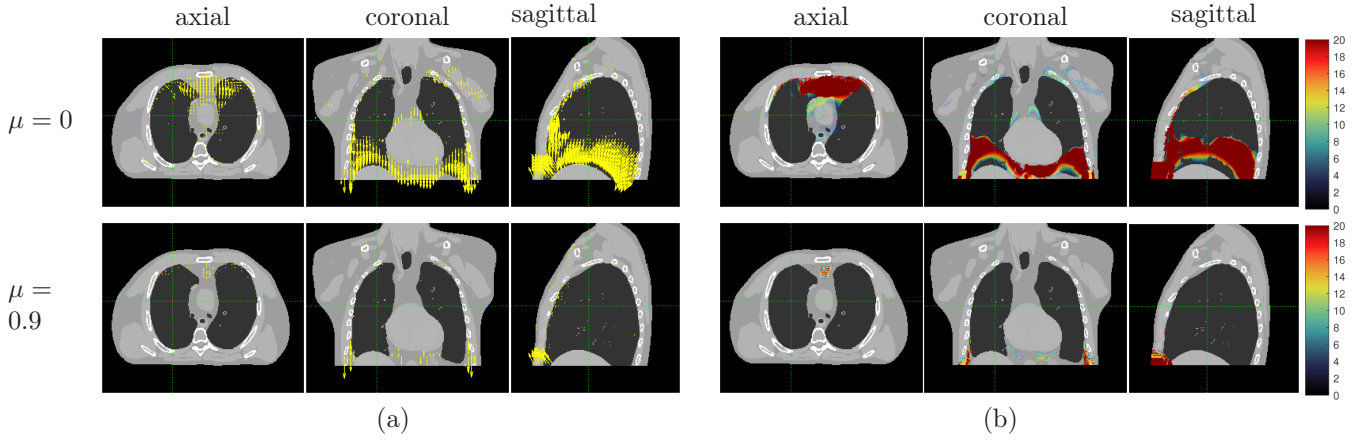


Figure 10: Residual error maps for inversion of the XCAT-phantom DVF. (a) Voxel-wise residual error vectors (yellow). Residual error vectors with length ≥ 0.1 mm. (b) Voxel-wise residual error amplitudes (semi-transparent heat-map overlay). Overlay opacity is proportional to voxel-wise error amplitudes. The top and bottom residual maps correspond to 60 iterations with feedback control parameter $\mu = 0$ and $\mu = 0.9$, respectively.

improve convergence behavior. We have described and demonstrated the key principle for altering and controlling error propagation, and a methodology for determining the control parameters numerically as well as analytically. Experimental results are in agreement with the presented error analysis and control design objectives. We give below some additional comments on computational issues and extended feedback control mechanisms.

4.1 Alternative iteration formula

The iteration (9) can be described alternatively as the following procedure with two sub-steps per iteration,

$$\mathbf{G}_{k+\frac{1}{2}}(\mathbf{x}) = -\mathbf{F}(\mathbf{x} + \mathbf{G}_k(\mathbf{x})), \quad (19a)$$

$$\mathbf{G}_{k+1}(\mathbf{x}) = (\mathbf{I} - \mathbf{B}(\mathbf{x})) \cdot \mathbf{G}_k(\mathbf{x}) + \mathbf{B}(\mathbf{x}) \cdot \mathbf{G}_{k+\frac{1}{2}}(\mathbf{x}). \quad (19b)$$

The first sub-step ($k + \frac{1}{2}$) is the same as Chen’s iteration. The second sub-step makes a modification by a combination of the estimates at step k and sub-step ($k + \frac{1}{2}$). The alternative computation procedure is mathematically equivalent with respect to convergence analysis, to iteration (9), although the residual feedback is not used explicitly.

4.2 Termination criteria

The residuals can be effectively utilized in termination criteria. Commonly used termination criteria include a threshold on the numerical difference between two successive iterates and an upper bound on the total number of iteration steps. The threshold is set based on an acceptable precision in computed results, and it should not be set higher than the computational precision used, such as IEEE single or double precision. A process is terminated by the numerical threshold criterion either

because the iteration has converged numerically, or because its progression is too slow. We would need an additional indicator to differentiate the two cases. Recall that the residual is related, but not necessarily equal, to the difference between successive iterates. If the residual is not sufficiently small, the estimate is far from meeting the inverse consistency condition and the iteration has not converged well enough.

4.3 Adaptive feedback control

The single-parameter feedback control described in section 2.1 is simple. The parameter μ is kept constant over the spatial domain and across all iteration steps. While this simple control mechanism proved effective with the analytic and XCAT DVF data used in this study, the robustness of the convergence can be further improved by extending the control in the following two approaches.

The first extension is to turn the constant parameter to a spatially variant control function $\mu(\mathbf{x})$. In fact, by the error propagation analysis specific to the analytic DVF (11), an ideal control scheme is spatially-variant, $\mu(\theta) = -b \cos(m\theta)$. Both analysis and numerical results (not presented in this paper) show that the iteration with $\mu(\theta)$ takes only one or two steps for the residuals to drop to numerical zero, as determined by the machine precision. Since the residual is vector-valued in general, a spatially-variant control function $\mathbf{B}(\mathbf{x})$ with 3×3 matrix local to each \mathbf{x} can be used. The second extension is to make the control non-stationary, i.e., to allow changes throughout the iteration process in adaptation to changes in the iterates or residuals.

Acknowledgements

This work was supported by the National Institutes of Health Grant No. R01-CA184173. The authors thank

Dr. Paul Segars and Wendy Harris for their insightful suggestions on generating the XCAT phantom. They thank Animesh Srivastava for his generous time and effort on technical assistance.

Disclosure of conflicts of interest

The authors have no relevant conflicts of interest to disclose.

A Error propagation equation for analytical DVF

We give the derivation of error propagation equations presented in this paper. Denote the error in estimating the DVF inverse at iteration k by $E_k(\mathbf{x})$.

$$\begin{aligned}
\mathbf{E}_{k+1}(\mathbf{x}) &= \hat{\mathbf{G}}_{k+1}(\mathbf{x}) - \mathbf{G}(\mathbf{x}) \\
&= \hat{\mathbf{G}}_k(\mathbf{x}) - \mathbf{G}(\mathbf{x}) - (1 - \mu) \left(\hat{\mathbf{G}}_k(\mathbf{x}) + \mathbf{F}(\mathbf{x} + \hat{\mathbf{G}}_k(\mathbf{x})) \right) \\
&= \mathbf{E}_k(\mathbf{x}) - (1 - \mu) \left(\mathbf{G}_k + \mathbf{F}(\mathbf{x} + \hat{\mathbf{G}}_k(\mathbf{x})) \right) \\
&= \mathbf{E}_k(\mathbf{x}) - (1 - \mu) \left(\mathbf{E}_k(\mathbf{x}) + \mathbf{G}(\mathbf{x}) + \mathbf{F}(\mathbf{x} + \hat{\mathbf{G}}_k(\mathbf{x})) \right) \\
&= \mathbf{E}_k(\mathbf{x}) - (1 - \mu) \left(\mathbf{E}_k(\mathbf{x}) - \mathbf{F}(\mathbf{x} + \mathbf{G}(\mathbf{x})) + \mathbf{F}(\mathbf{x} + \hat{\mathbf{G}}_k(\mathbf{x})) \right)
\end{aligned} \tag{20}$$

For the analytical phantom of (11),

$$\begin{aligned}
&\mathbf{F}(\mathbf{x} + \hat{\mathbf{G}}_k(\mathbf{x})) - \mathbf{F}(\mathbf{x} + \mathbf{G}(\mathbf{x})) \\
&= \left(\frac{1}{1 + b \cos(m\theta)} - 1 \right) \left(\hat{\mathbf{G}}_k(\mathbf{x}) - \mathbf{G}(\mathbf{x}) \right),
\end{aligned} \tag{21}$$

which gives the specific error propagation equation (12),

$$\mathbf{E}_{k+1}(\mathbf{x}) = \left(1 - (1 - \mu) \frac{1}{1 + b \cos(m\theta)} \right) \mathbf{E}_k(\mathbf{x}). \tag{22}$$

B Error propagation equation (general form)

For general DVF, using first order Taylor expansion,

$$\mathbf{F}(\mathbf{x} + \hat{\mathbf{G}}_k(\mathbf{x})) - \mathbf{F}(\mathbf{x} + \mathbf{G}(\mathbf{x})) = J_{\mathbf{F}}(\tilde{\mathbf{x}}) \left(\hat{\mathbf{G}}_k(\mathbf{x}) - \mathbf{G}(\mathbf{x}) \right) \tag{23}$$

where $\tilde{\mathbf{x}} \in (\mathbf{x} + \mathbf{G}(\mathbf{x}), \mathbf{x} + \hat{\mathbf{G}}_k(\mathbf{x}))$. This gives the error propagation equation of (15a),

$$\mathbf{E}_{k+1}(\mathbf{x}) = (I - (1 - \mu)(I + J_{\mathbf{F}}(\tilde{\mathbf{x}}))) \mathbf{E}_k(\mathbf{x}). \tag{24}$$

C Convergence condition

The necessary and sufficient condition of the convergence of iteration process (10) is,

$$\begin{aligned}
-1 &< 1 - (1 - \mu) \frac{1}{1 + b \cos(m\theta)} < 1, \quad \forall \theta \\
\iff -1 &< \frac{\mu + b \cos(m\theta)}{1 + b \cos(m\theta)} < 1, \quad \forall \theta \\
\iff -(1 + 2b \cos(m\theta)) &< \mu < 1, \quad \forall \theta \\
\iff 2b - 1 &< \mu < 1.
\end{aligned} \tag{25}$$

D Optimal control parameter

We derive the optimal μ in convergence rate for the analytical phantom (11).

$$\begin{aligned}
\mu_{opt} &= \arg \min_{\mu} \max_{\theta \in [0, 2\pi]} \left(1 - (1 - \mu) \frac{1}{1 + b \cos(m\theta)} \right)^2 \\
&= \arg \min_{\mu} \max_{y \in [-b, b]} \left(1 - \frac{1 - \mu}{1 + y} \right)^2 \\
&= \arg \min_{\mu} \begin{cases} \left(\frac{\mu - b}{1 - b} \right)^2, & \mu \leq b^2 \\ \left(\frac{\mu + b}{1 + b} \right)^2, & \mu > b^2 \end{cases} \\
&= b^2
\end{aligned} \tag{26}$$

References

- [1] M. Chen, W. Lu, Q. Chen, K. J. Ruchala, and G. H. Olivera. A simple fixed-point approach to invert a deformation field. *Medical physics*, 35(1):81–88, 2008.
- [2] G. E. Christensen and H. J. Johnson. Consistent image registration. *Medical Imaging, IEEE Transactions on*, 20(7):568–582, 2001.
- [3] A. Leow, S.-C. Huang, A. Geng, J. Becker, S. Davis, A. Toga, and P. Thompson. Inverse consistent mapping in 3D deformable image registration: its construction and statistical properties. In *Information Processing in Medical Imaging*, pages 493–503. Springer, 2005.
- [4] W. Lu, G. H. Olivera, Q. Chen, K. J. Ruchala, J. Haimler, S. L. Meeks, K. M. Langen, and P. A. Kupelian. Deformable registration of the planning image (kvct) and the daily images (mvct) for adaptive radiation therapy. This work was in part presented at the aapm meeting in seattle, july 2005. *Physics in medicine and biology*, 51(17):4357, 2006.
- [5] L. Ren, Y. Zhang, and F.-F. Yin. A limited-angle intrafraction verification (live) system for radiation therapy. *Medical physics*, 41(2):020701, 2014.

- [6] W. P. Segars, M. Mahesh, T. J. Beck, E. C. Frey, and B. M. W. Tsui. Realistic CT simulation using the 4D XCAT phantom. *Medical Physics*, 35(8):3800, 2008.
- [7] Y. Seppenwoolde, H. Shirato, K. Kitamura, S. Shimizu, M. van Herk, J. V. Lebesque, and K. Miyasaka. Precise and real-time measurement of 3d tumor motion in lung due to breathing and heart-beat, measured during radiotherapy. *International Journal of Radiation Oncology* Biology* Physics*, 53(4):822–834, 2002.
- [8] A. Sotiras, C. Davatzikos, and N. Paragios. Deformable medical image registration: a survey. *IEEE Transactions on Medical Imaging*, 32(7):1153–1190, July 2013.
- [9] D. Yan, F. Vicini, J. Wong, and A. Martinez. Adaptive radiation therapy. *Physics in medicine and biology*, 42(1):123, 1997.